Int. J. Solids Structures Vol. 23, No. 7, pp. 871–896, 1987
Printed in Great Britain.

0020-7683/87 $3.00+ .00

LOW VELOCITY IMPACT OF TRANSVERSELY ISOTROPIC BEAMS AND PLATES

W. P. SCHONBERG, L. M. KEER and T. K. WOO
Department of Civil Engineering, Northwestern University, Evanston, IL 60201, U.S.A.

(*Received* 15 *April* 1986; *in revised form* 22 *August* 1986)

Abstract—The dynamic structural contact problems of a rigid, smooth cylindrical striker impacting an elastically supported transversely isotropic beam and plate are solved. The solutions are obtained as a superposition of a static layer solution derived through the use of integral transforms with an elementary beam or plate theory solution that incorporates the dynamic effects. The problems are formulated in such a manner as to require the solution of a Volterra integral equation for each time step. Numerical results are presented for fixed and simply supported beams and plates. Three materials are used to study the effects of anisotropy: magnesium, which is nearly isotropic; cadmium, which is moderately anisotropic; and graphite/epoxy, which is highly anisotropic.

1. INTRODUCTION

The transverse impact of beams and plates has long been a problem of theoretical and practical interest in applied mechanics research. Dynamic impact theory has been used to model and study a variety of impact phenomena, including studies of car impact on highway guardrails[1], structural response to blast loadings such as sonic booms[2] and shot peening[3, 4], delamination of composite members due to impact[5], erosion of metal surfaces by solid particle impact[6, 7], and impact response of gears and turbine blades[8]. These studies approximated local impact stresses with Hertzian stress distributions. However, prior static and dynamic beam and plate indentation studies[9–14] have shown that these local stresses will differ significantly from Hertzian distributions when the contact region is relatively large. Consequently, a wide variety of local effects that can significantly influence dynamic response[15] have been systematically neglected.

The purpose of this study is to extend the technique used in the static beam and plate indentation studies to problems of dynamic indentation. In this manner the forthcoming solution will account for the global behavior of the beam or plate and will include the effects of local impact stresses and strains as well.

2. SECTION I: DYNAMIC IMPACT OF A FINITE BEAM

2.1. *Introduction*

In this section we examine the low velocity impact of a rigid cylindrical projectile on a finite elastically supported transversely isotropic beam. The geometry of the problem is shown in Fig. 1. Only low velocity impact is considered in order to avoid complications

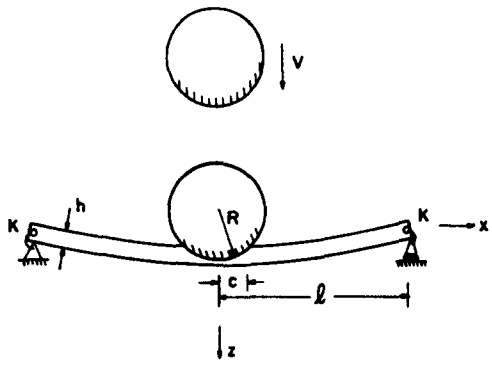

Fig. 1. Problem configuration.

that may result from high velocity impact, such as puncture or penetration. In this manner, local deformations between the impactor and the beam can be said to occur elastically[16]. If the impact velocity is low enough, the deformations can be assumed to occur quasi-statically. Under this assumption, elastodynamic effects are negligible when compared to dynamic beam effects and are therefore neglected. It has been shown[17, 18] that such presumptions are permissible under the circumstances of the problem and do not adversely affect the accuracy of the results.

The solution to the present problem is obtained as the superposition of an elasticity layer solution with two beam theory solutions, one static and one dynamic. The superposition of the elasticity solution with the static beam solution results in a static solution similar to the one developed by Keer and Ballarini[10]. The dynamic beam theory solution is a standard solution that incorporates structural dynamic effects[19]. Although the static component, which gives local stresses, is often neglected in the study of impact phenomena, it is expected that in cases of large area contact its contribution will be the same order of magnitude as that derived from the dynamic bending solution. Furthermore, the static solution gives an accurate representation of the contact phenomenon, including the local stresses as well as the behavior near the edges of the contact region. The static component must therefore be included in the analysis. Superposition of the two solutions and the matching of boundary conditions lead to a Volterra integral equation of the second kind. The unknown contact length and pressure distribution at each instant of time are obtained using a technique that combines a standard numerical scheme for Volterra integral equations[20] with the technique developed by Ahmadi *et al.*[21] for the solution of non-Hertzian contact problems. Once the contact pressure is obtained, then all relative field quantities can be readily calculated. By varying the initial impact velocity and the ratio of beam mass to projectile mass, an extensive study of the response of a transversely isotropic beam to low velocity impact is performed. To assess the effects of anisotropy on the beam's response, solutions are obtained for three materials: magnesium, which is nearly isotropic; cadmium, which is highly anisotropic; and unidirectional graphite/epoxy, the elastic properties of which are assumed to be representable by a transversely isotropic material[22].

It should be noted that because the impact velocity is low and we are sampling bending stresses at midspan, the approximations of Euler–Bernoulli beam theory are valid and its use in the construction of the static layer solution should yield accurate results[23, 24]. Furthermore, because the duration of impact is expected to be of the same order of magnitude as the fundamental period of vibration of the beam, it again follows that the use of the Euler–Bernoulli beam theory should yield satisfactory results[25–28]. However, if the impact were sharp and the duration of contact very short, or if we were sampling shear stresses at the supports, then Euler–Bernoulli beam theory approximations would lose their validity and Timoshenko beam theory would have to be used instead[29–32].

2.2. *Problem formulation*

2.2.1. *Static solution.* The boundary conditions for the layer solution are those of an elastically supported layer of thickness h loaded on the upper surface by a smooth symmetric rigid indenter (see Fig. 1)

$$\tau_{zz}(x, h) = 0, \qquad |x| < \infty \tag{1}$$

$$\tau_{xz}(x, h) = 0, \qquad |x| < \infty \tag{2}$$

$$\tau_{xz}(x, 0) = 0, \qquad |x| < \infty \tag{3}$$

$$\tau_{zz}(x, 0) = 0, \qquad c < |x| < \infty \tag{4}$$

$$\tau_{zz}(x, 0) = -p(x), \qquad 0 < |x| < c \tag{5}$$

where c is the semi-contact length and $p(x)$ is the loading due to the indenter. The static

beam theory boundary conditions are those of an elastically supported beam and are given by

$$u_z = 0, \qquad M - K\bar{\theta} = 0, \qquad x = l \tag{6,7}$$

where l is the half-length of the beam, M the bending moment, K the elastic spring constant at the ends of the beam, and $\bar{\theta}$ is the value of the slope averaged through the thickness

$$\bar{\theta} = \frac{1}{h}\int_0^h \frac{\partial u_z}{\partial x}\,\mathrm{d}z. \tag{8}$$

A suitable elasticity solution that represents a general loading on the upper surface of an elastic, transversely isotropic layer and no loading on the lower surface can be obtained using the techniques of Green and Zerna[33], and Sneddon[34], and is found to be

$$\tau_{zz} = \int_0^\infty \frac{E(\xi)\cos(\xi x)}{D(\xi)}\{\sqrt{\nu_1}\,I(\xi)\cosh(\xi z/\sqrt{\nu_1}) + \sqrt{\nu_2}H(\xi)\cosh(\xi z/\sqrt{\nu_2}) - G(\xi)[\sqrt{\nu_1}\sinh(\xi z/\sqrt{\nu_1}) - \sqrt{\nu_2}\sinh(\xi z/\sqrt{\nu_2})]\}\,\mathrm{d}\xi \tag{9}$$

$$\tau_{xz} = -\int_0^\infty \frac{E(\xi)\sin(\xi x)}{D(\xi)}\{I(\xi)\sinh(\xi z/\sqrt{\nu_1}) + H(\xi)\sinh(\xi z/\sqrt{\nu_2}) - G(\xi)[\cosh(\xi z/\sqrt{\nu_1}) - \cosh(\xi z/\sqrt{\nu_2})]\}\,\mathrm{d}\xi \tag{10}$$

$$\tau_{xx} = \int_0^\infty \frac{E(\xi)\cos(\xi x)}{D(\xi)}\left\{-\frac{I(\xi)}{\sqrt{\nu_1}}\cosh(\xi z/\sqrt{\nu_1}) - \frac{H(\xi)}{\sqrt{\nu_2}}\cosh(\xi z/\sqrt{\nu_2}) + G(\xi)\left[\frac{1}{\sqrt{\nu_1}}\sinh(\xi z/\sqrt{\nu_1}) - \frac{1}{\sqrt{\nu_2}}\sinh(\xi z/\sqrt{\nu_2})\right]\right\}\mathrm{d}\xi \tag{11}$$

$$u_z = \frac{1}{c_{44}}\int_0^\infty \frac{E(\xi)\cos(\xi x)}{\xi D(\xi)}\left\{\frac{\kappa_1 I(\xi)}{1+\kappa_1}\sinh(\xi z/\sqrt{\nu_1}) + \frac{\kappa_2 H(\xi)}{1+\kappa_2}\sinh(\xi z/\sqrt{\nu_2}) - G(\xi)\left[\frac{\kappa_1}{1+\kappa_1}\cosh(\xi z/\sqrt{\nu_1}) - \frac{\kappa_2}{1+\kappa_2}\cosh(\xi z/\sqrt{\nu_2})\right]\right\}\mathrm{d}\xi \tag{12}$$

$$u_x = -\frac{1}{c_{44}}\int_0^\infty \frac{E(\xi)\sin(\xi x)}{\xi D(\xi)}\left\{\frac{I(\xi)\sqrt{\nu_1}}{1+\kappa_1}\cosh(\xi z/\sqrt{\nu_1}) + \frac{H(\xi)\sqrt{\nu_2}}{1+\kappa_2}\cosh(\xi z/\sqrt{\nu_2}) - G(\xi)\left[\frac{\sqrt{\nu_1}}{1+\kappa_1}\sinh(\xi z/\sqrt{\nu_1}) - \frac{\sqrt{\nu_2}}{1+\kappa_2}\sinh(\xi z/\sqrt{\nu_2})\right]\right\}\mathrm{d}\xi \tag{13}$$

where

$$D(\xi) = 2\sqrt{\nu_2}(\mathrm{ch}\,\beta_1\,\mathrm{ch}\,\beta_2 - 1) - \frac{\nu_1+\nu_2}{\sqrt{\nu_1}}\mathrm{sh}\,\beta_1\,\mathrm{sh}\,\beta_2 \tag{14}$$

$$G(\xi) = \sqrt{\left(\frac{\nu_2}{\nu_1}\right)}\mathrm{ch}\,\beta_2\,\mathrm{sh}\,\beta_1 - \mathrm{ch}\,\beta_1\,\mathrm{sh}\,\beta_2 \tag{15}$$

$$H(\xi) = \operatorname{ch}\beta_1 \operatorname{ch}\beta_2 - \sqrt{\left(\frac{\nu_2}{\nu_1}\right)} \operatorname{sh}\beta_1 \operatorname{sh}\beta_2 - 1 \tag{16}$$

$$I(\xi) = \sqrt{\left(\frac{\nu_2}{\nu_1}\right)} (\operatorname{ch}\beta_1 \operatorname{ch}\beta_2 - 1) - \operatorname{sh}\beta_1 \operatorname{sh}\beta_2 \tag{17}$$

and $\beta_i = \xi h/\sqrt{\nu_i}$; $E(\xi)$ is an as yet unknown function of the applied loading. The material constants ν_i and κ_i are obtained using the technique outlined in Ref. [33]. The ν_i are the roots of the equation

$$K_{44}K_{11}\nu^2 - (K_{11}K_{33} - K_{13}^2 - 2K_{13}K_{44})\nu + K_{44}K_{33} = 0 \tag{18}$$

where the K_{ij} are constant functions of the layer moduli c_{ij} and whether the layer is in a state of plane strain or plane stress. If a state of plane strain is assumed, then $K_{ij} = c_{ij}$; if plane stress is assumed, then $K_{11} = c_{11} - c_{12}^2/c_{11}$, $K_{13} = c_{13} - c_{12}c_{13}/c_{11}$, $K_{33} = c_{33} - c_{13}^2/c_{11}$, and $K_{44} = c_{44}$.

It is seen that on $z = h$ the normal and shear stresses vanish automatically as does the shear stress on $z = 0$. The normal stress on $z = 0$ is given as

$$\tau_{zz}(x, 0) = \int_0^\infty E(\xi) \cos(\xi x)\, \mathrm{d}\xi. \tag{19}$$

Substituting eqn (19) into eqns (4) and (5) and applying a Fourier cosine transform yields

$$E(\xi) = -\frac{2}{\pi} \int_0^c p(x) \cos(\xi x)\, \mathrm{d}x. \tag{20}$$

The moment and average slope due to this layer solution are found to be

$$M_E = \int_0^h z\tau_{xx}\, \mathrm{d}z = -\int_0^\infty \xi^{-2} E(\xi) \cos(\xi x)\, \mathrm{d}\xi \tag{21}$$

$$\bar{\theta}_E = \frac{1}{h} \int_0^h \frac{\partial u_z}{\partial x}\, \mathrm{d}z = \frac{\sqrt{\nu_2}}{c_{44}} \int_0^\infty \frac{E(\xi)F(\xi)}{\xi D(\xi)} \sin(\xi x)\, \mathrm{d}\xi \tag{22}$$

where

$$F(\xi) = \left(\frac{\kappa_1}{1+\kappa_1} + \frac{\kappa_2}{1+\kappa_2}\right)(\operatorname{ch}\beta_1 \operatorname{ch}\beta_2 - 1) - \left[\frac{\kappa_1}{1+\kappa_1}\sqrt{\left(\frac{\nu_1}{\nu_2}\right)} + \frac{\kappa_2}{1+\kappa_2}\sqrt{\left(\frac{\nu_2}{\nu_1}\right)}\right] \operatorname{sh}\beta_1 \operatorname{sh}\beta_2$$
$$+ \left(\frac{\kappa_1}{1+\kappa_1} - \frac{\kappa_2}{1+\kappa_2}\right)(\operatorname{ch}\beta_1 - \operatorname{ch}\beta_2). \tag{23}$$

The static beam theory solution is taken in the form of a quadratic pure bending displacement solution by

$$u_z(x) = \frac{1}{2}Ax^2 + B. \tag{24}$$

Assuming the hypotheses of the Euler–Bernoulli beam theory, the following expression for moment and average slope are obtained:

$$M_B = -D^*A \tag{25}$$

$$\theta_B = Ax \tag{26}$$

where $D^* = h^3(c_{11}-c_{13}^2/c_{33})(1-n^2)/12$, with $n = 0$ for plane strain and $n = (c_{12}-c_{13}^2/c_{33})/(c_{11}-c_{13}^2/c_{33})$ for plane stress. The constants A and B are obtained by superimposing appropriate beam theory expressions with corresponding elasticity expressions and applying the beam theory boundary conditions given by eqns (6) and (7). The resulting expressions are

$$A = -\frac{1}{D^*(1+\alpha^*)}\int_0^\infty E(\xi)\left[\frac{\cos(\xi l)}{\xi^2} + \frac{\alpha^* D^*\sqrt{\nu_2}}{c_{44}hl}\frac{F(\xi)}{D(\xi)}\frac{\sin(\xi l)}{\xi}\right]d\xi \tag{27}$$

$$B = \frac{1}{D^*}\int_0^\infty E(\xi)\left[\frac{l^2}{2(1+\alpha^*)}\frac{\cos(\xi l)}{\xi^2} + \frac{D^*\sqrt{\nu_2}\,l}{2c_{44}h}\frac{\alpha^*}{1+\alpha^*}\frac{F(\xi)}{D(\xi)}\frac{\sin(\xi l)}{\xi} + \frac{D^*}{c_{44}}\left(\frac{\kappa_1}{1+\kappa_1}-\frac{\kappa_2}{1+\kappa_2}\right)\frac{G(\xi)}{D(\xi)}\frac{\cos(\xi l)}{\xi}\right]d\xi \tag{28}$$

where $\alpha^* = Kl/D^*$ is a dimensionless parameter measuring support stiffness.

Superposing eqns (12) and (24) and making use of eqns (20), (27) and (28), the total displacement as expressed in terms of $p(x)$ is

$$u_z(x,0) = \frac{1}{\pi D^*}\int_0^c p(x')\int_0^\infty \left\{\frac{2D^*}{c_{44}}\left(\frac{\kappa_1}{1+\kappa_1}-\frac{\kappa_2}{1+\kappa_2}\right)\frac{G(\xi)}{D(\xi)}\frac{\cos(\xi x)-\cos(\xi l)}{\xi} - \frac{l^2-x^2}{1+\alpha^*}\left[\frac{\cos(\xi l)}{\xi^2} + \frac{\alpha^* D^*\sqrt{\nu_2}}{hlc_{44}}\frac{F(\xi)}{D(\xi)}\frac{\sin(\xi l)}{\xi}\right]\cos\xi x'\right\}d\xi\,dx' \tag{29}$$

where the difference $|u_z(x,0)-u_z(x,h)|$ is assumed to be negligibly small.

It is seen from an asymptotic analysis that the integrand in curly brackets is bounded as $\xi \to 0$, but is unbounded as $\xi \to \infty$. After adjusting the improper behavior at infinity, eqn (29) becomes

$$u_z(x,0) = -\frac{1}{\pi}\int_0^c p(x')\left[\delta_1 \log\frac{|x+x'||x-x'|}{|l+x'||l-x'|} + \delta_2\frac{\pi\alpha^*}{1+\alpha^*}\frac{l^2-x^2}{2hl}\right]dx' + \frac{1}{\pi D^*}\int_0^c p(x')K(x,x')\,dx' \tag{30}$$

where

$$\delta_1 = \frac{1}{c_{44}}\left(\frac{\kappa_1}{1+\kappa_1}-\frac{\kappa_2}{1+\kappa_2}\right)\frac{1}{\sqrt{\nu_1}-\sqrt{\nu_2}} \tag{31}$$

$$\delta_2 = \frac{1}{c_{44}}\left(\frac{\kappa_1\sqrt{\nu_1}}{1+\kappa_1}-\frac{\kappa_2\sqrt{\nu_2}}{1+\kappa_2}\right)\frac{1}{\sqrt{\nu_1}-\sqrt{\nu_2}} \tag{32}$$

$$K(x,x') = \int_0^\infty \cos(\xi x')\left\{\frac{2D^*}{c_{44}}\left(\frac{\kappa_1}{1+\kappa_1}-\frac{\kappa_2}{1+\kappa_2}\right)\left[\frac{G(\xi)}{D(\xi)}-\frac{1}{\sqrt{\nu_1}-\sqrt{\nu_2}}\right]\frac{\cos(\xi x)-\cos(\xi l)}{\xi} - \frac{l^2-x^2}{1+\alpha^*}\left(\frac{\cos(\xi l)}{\xi^2} + \frac{\alpha^* D^*}{hl}\left[\frac{\sqrt{\nu_2}}{c_{44}}\frac{F(\xi)}{D(\xi)}-\delta_2\right]\frac{\sin(\xi l)}{\xi}\right)\right\}d\xi. \tag{33}$$

2.2.2. *Dynamic beam theory solution.* We assume that the pressure distribution is symmetric with respect to $x = 0$ so that only the right half of the beam (i.e. $0 < x < l$) is considered. By using a Laplace transform technique and a normal mode expansion[19], the deflection of a transversely isotropic beam initially at rest is found to be

$$u_z(x,t) = \frac{1}{\rho h}\sum_{n=1}^{\infty}\frac{Y_n(x)}{\omega_n^*}\int_0^l Y_n(x')\int_0^t p(x',\tau)\sin[\omega_n^*(t-\tau)]\,d\tau\,dx' \tag{34}$$

where $\omega_n^* = \beta_n^2\sqrt{(D^*/\rho h)}$ and ρ is the mass density of the beam material. Expressions for the natural frequencies β_n and normal modes Y_n considered are given for arbitrary α^* by eqns (34)–(37) in Ref. [14].

2.2.3. *Superposition solution—integral equation for the dynamic problem.* Superposing eqns (30) and (34), the total dynamic displacement is given by

$$u_z(x,0,t) = -\frac{1}{\pi}\int_0^{c(t)} p(x')\left[\delta_1\log\frac{|x+x'||x-x'|}{|l+x'||l-x'|} + \delta_2\frac{\pi\alpha^*}{1+\alpha^*}\frac{l^2-x^2}{2hl}\right]dx'$$
$$+\frac{1}{\pi D^*}\int_0^{c(t)} p(x')K(x,x')\,dx' + \frac{1}{\rho h}\int_0^t\int_0^{c(\tau)} p(x',\tau)\sum_{n=1}^{\infty}\frac{Y_n(x)Y_n(x')}{\omega_n^*}$$
$$\times\sin[\omega_n^*(t-\tau)]\,dx'\,d\tau. \tag{35}$$

In the contact region, we have

$$u_z(x,0,t) = \Delta(t) - x^2/2R, \qquad 0 < x < c(t) \tag{36}$$

where $\Delta(t)$ is the relative approach (a function of time, as is the contact region) and R is the radius of curvature of the projectile. An additional equation is obtained from Newton's equation of motion

$$m_p\frac{\partial^2\Delta}{\partial t^2} = -2\int_0^{c(t)} p(x,t)\,dx \tag{37}$$

where m_p is the mass of the projectile per unit length. If the projectile has an initial velocity V, then eqn (37) can be integrated twice to yield

$$\Delta(t) = Vt - \frac{M}{\rho hl}\int_0^t (t-\tau)\int_0^{c(\tau)} p(x',\tau)\,dx'\,d\tau \tag{38}$$

where M is the ratio of the mass of the beam to that of the projectile. Substituting eqns (36) and (38) into eqn (35) and rearranging terms yields the integral equation in $p(x,t)$ for the impact problem

$$\frac{1}{\pi D^*}\int_0^{c(t)} p(x',t)K(x,x')\,dx' - \frac{1}{\pi}\int_0^{c(t)} p(x',t)L(x,x')\,dx'$$
$$+\frac{1}{\rho h}\int_0^t\int_0^{c(\tau)} p(x',\tau)M(x,x',\tau)\,dx'\,d\tau + \frac{M}{\rho hl}\int_0^t (t-\tau)\int_0^{c(\tau)} p(x',\tau)\,dx'\,d\tau$$
$$= Vt - x^2/2R \tag{39}$$

where

$$L(x,x') = \delta_1 \log \frac{|x+x'||x-x'|}{|l+x'||l-x'|} + \delta_2 \frac{\pi\alpha^*}{1+\alpha^*} \frac{l^2-x^2}{2hl} \tag{40}$$

$$M(x,x',\tau) = \sum_{n=1}^{\infty} \frac{Y_n(x)Y_n(x')}{\omega_n^*} \sin[\omega_n^*(t-\tau)]. \tag{41}$$

2.3. *Numerical solution*

In solving eqn (39) numerically, first the order of integration and summation is interchanged. Expanding the kernel $M(x,x',\tau)$ and rearranging yields

$$\begin{aligned}
&\frac{1}{\pi D^*}\int_0^{c(t)} p(x',t)K(x,x')\,dx' - \frac{1}{\pi}\int_0^{c(t)} p(x',t)L(x,x')\,dx' \\
&\quad + \frac{1}{\rho h}\sum_{n=1}^{\infty}\frac{Y_n(x)}{\omega_n^*}\left\{\sin(\omega_n^* t)\int_0^t \cos(\omega_n^*\tau)\left[\int_0^{c(\tau)} p(x',\tau)Y_n(x')\,dx'\right]d\tau\right. \\
&\quad \left. -\cos(\omega_n^* t)\int_0^t \sin(\omega_n^*\tau)\left[\int_0^{c(\tau)} p(x',\tau)Y_n(x')\,dx'\right]d\tau\right\} \\
&\quad + \frac{M}{\rho hl}\int_0^t (t-\tau)\left[\int_0^{c(\tau)} p(x',\tau)\,dx'\right]d\tau = Vt - x^2/2R.
\end{aligned} \tag{42}$$

For the integration over time, the domain is partitioned into evenly spaced intervals. Then, at time-step t_k eqn (42) can be written as

$$\begin{aligned}
&\int_0^{c_k} p(x',t_k)Q(x,x')\,dx' + \frac{1}{\rho h}\sum_{n=1}^{\infty}\frac{Y_n(x)}{\omega_n^*}\left\{\sin(\omega_n^* t_k)\int_0^{t_k} f_n(\tau)\cos(\omega_n^*\tau)\,d\tau\right. \\
&\qquad \left. -\cos(\omega_n^* t_k)\int_0^{t_k} f_n(\tau)\sin(\omega_n^*\tau)\,d\tau\right\} + \frac{M}{\rho hl}\int_0^{t_k}(t_k-\tau)g(\tau)\,d\tau \\
&\qquad = Vt_k - x^2/2R
\end{aligned} \tag{43}$$

where

$$Q(x,x') = \frac{1}{\pi D^*}K(x,x') - \frac{1}{\pi}L(x,x') \tag{44}$$

$$f_n(\tau) = \int_0^{c(\tau)} p(x',\tau)Y_n(x')\,dx' \tag{45}$$

$$g(\tau) = \int_0^{c(\tau)} p(x',\tau)\,dx' \tag{46}$$

and $c_k = c(t_k)$. Performing the integration over time numerically, eqn (43) is rewritten as

$$\begin{aligned}
&\int_0^{c_k} p(x',t_k)Q(x,x')\,dx' + \frac{1}{\rho h}\sum_{n=1}^{\infty}\frac{Y_n(x)}{\omega_n^*}\left\{\sin(\omega_n^* t_k)\sum_{l=1}^{k} w_{kl}^c f_n(t_l)\right. \\
&\qquad \left. -\cos(\omega_n^* t_k)\sum_{l=1}^{k} w_{kl}^s f_n(t_l)\right\} + \frac{M}{\rho hl}\sum_{l=1}^{k} w_{kl}^i g(t_l) = Vt_k - x^2/2R
\end{aligned} \tag{47}$$

where

$$f_n(t_l) = \int_0^{c_l} p(x', t_l) Y_n(x') \, dx' \tag{48}$$

$$g(t_l) = \int_0^{c_l} p(x', t_l) \, dx' \tag{49}$$

and w_{kl}^c, w_{kl}^s, w_{kl}^i are the weights of the integration scheme. The derivation of these weights is shown in the Appendix.

At each time-step, the contact length is divided into N equal segments of length Δx and overestimated. An iterative procedure[21] is then used to determine the actual contact length and pressure distribution for that time-step. In this procedure, the pressure distribution is assumed to be piecewise constant, that is

$$p(x, t_l) = p_j^{(l)}, \qquad x_j - \Delta x/2 \leqslant x \leqslant x_j + \Delta x/2 \tag{50}$$

where $x_j = (j-1/2)\Delta x, j = 1, 2, \ldots, N$. Under this assumption, eqns (48) and (49) become

$$f(t_l) = \sum_{j=1}^{N_l} p_j^{(l)} I_n(x_j) \tag{51}$$

$$g(t_l) = \sum_{j=1}^{N_l} p_j^{(l)} \tag{52}$$

where

$$I_n(x_j) = \int_{x_j - \Delta x/2}^{x_j + \Delta x/2} Y_n(x') \, dx' \tag{53}$$

and N_l is the number of segments in the contact length of the lth time-step. Substituting eqns (51) and (52) into eqn (47) yields the discretized form of the integral equation for the dynamic impact problem

$$\sum_{j=1}^{N_k} S(x_i, x_j) p_j^{(k)} + \sum_{l=1}^{k} \left\{ \sum_{j=1}^{N_l} \left(\frac{1}{\rho h} \sum_{n=1}^{\infty} \left[\frac{Y_n(x_i) I_n(x_j)}{\omega_n^*} W_{kl}^{(n)} \right] p_j^{(l)} \right) \right\} + \frac{M}{\rho h l} \sum_{l=1}^{k} \left[\sum_{j=1}^{N_l} w_{kl}^i p_j^{(l)} \right] = V t_k - x_i^2/2R \tag{54}$$

where

$$W_{kl}^{(n)} = w_{kl}^c \sin(\omega_n^* t_k) - w_{kl}^s \cos(\omega_n^* t_k) \tag{55}$$

$$S(x_i, x_j) = \int_{x_j - \Delta x/2}^{x_j + \Delta x/2} Q(x_i, x') \, dx' \tag{56}$$

and $i = 1, 2, \ldots, N_k$.

As is typical of numerical solutions of Volterra integral equations, the scheme is a step-by-step one: the pressure distribution and contact length are unknown only in the current time-step. With this in mind, eqn (54) reduces to

Table 1. Elastic moduli (in N m^{-2})

	Magnesium	Cadmium	Graphite/epoxy
c_{11}	5.587×10^{10}	10.920×10^{10}	15.000×10^{10}
c_{12}	2.501×10^{10}	3.976×10^{10}	0.856×10^{10}
c_{13}	2.079×10^{10}	3.754×10^{10}	0.891×10^{10}
c_{33}	6.110×10^{10}	4.602×10^{10}	1.844×10^{10}
c_{44}	1.658×10^{10}	1.562×10^{10}	0.323×10^{10}

$$\sum_{j=1}^{N_k} A_{ij}^{(k)} p_j^{(k)} = B_i^{(k)}, \qquad i = 1,2,\ldots,N_k \tag{57}$$

where

$$A_{ij}^{(k)} = S(x_i,x_j) + \frac{1}{\rho h}\sum_{n=1}^{\infty}\frac{Y_n(x_i)I_n(x_j)}{\omega_n^*}W_{kk}^{(n)} + \frac{M}{\rho hl}(\Delta x)w_{kk}^{i} \tag{58}$$

$$B_i^{(k)} = Vt_k - x_i^2/2R - \sum_{l=1}^{k-1}\left\{\sum_{j=1}^{N_l}\left[\frac{1}{\rho h}\sum_{n=1}^{\infty}\frac{Y_n(x_i)I_n(x_j)}{\omega_n^*}W_{kl}^{(n)} + \frac{M}{\rho hl}(\Delta x)w_{kl}^{i}\right]p_j^{(l)}\right\}. \tag{59}$$

It should be noted that a numerical solution of a Volterra integral equation is highly sensitive to the starting value of the scheme. In order to reduce subsequent errors, the starting value is modified as suggested in Ref. [20]. The first and second time-steps are taken to be at time $t = \Delta t/4$ and $\Delta t/2$, respectively. After that, the solution proceeds in the usual manner.

2.4. *Elementary beam theory solutions*

The numerical results obtained in the solution of eqns (57)–(59) are compared with those obtained from an elementary beam theory analysis[35]. In this analysis it is assumed that the impact occurs inelastically and that the projectile and a certain portion of the beam mass impulsively attain the same velocity immediately after impact. It is further assumed that the dynamic transverse displacement is geometrically similar to the static displacement curve. Under these conditions, the maximum transverse displacement is found to be

$$u_{z,\max}^0 = V\tau/\sqrt{((\varepsilon M+1)M)} \tag{60}$$

and the duration of impact is

$$t^0 = \pi\tau\sqrt{((\varepsilon M+1)/M)} \tag{61}$$

where $\tau = \sqrt{(2\rho hl/k)}$, ε is the fraction of the beam mass that moves with the projectile at the same velocity after impact, k is the static load required to produce a unit deflection (i.e. the static stiffness) at the center of the beam, and V, M are as defined in eqn (38). The values of ε and k depend on the support conditions of the beam. For the end conditions in subsequent numerical calculations, they are given as follows:

simply supported ends $\qquad \varepsilon = 17/35, \quad k = 6D^*/l^3$ (62)

clamped ends $\qquad \varepsilon = 13/35, \quad k = 24D^*/l^3.$ (63)

2.5. *Observations and conclusions*

Three materials were chosen for this study: magnesium, cadmium and unidirectional graphite/epoxy. The elastic moduli of these materials are listed in Table 1. For each material, solutions were obtained for simply supported and clamped end conditions, and for impact velocities of 1 and 5 m s^{-1}; the mass ratio M was varied from 0.5 to 2.5. In each case, the

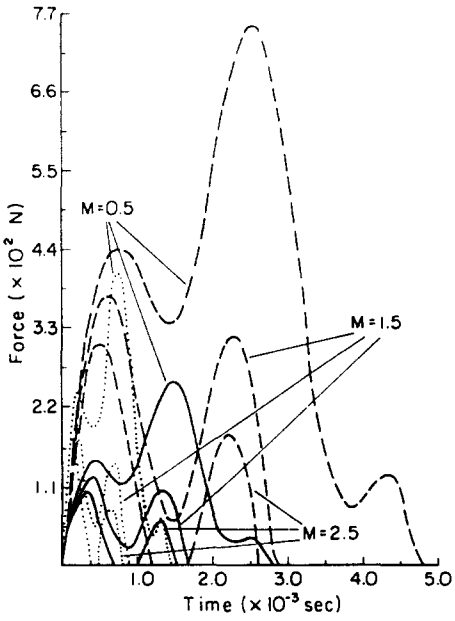

Fig. 2(a). Force history, simply supported beam, $V = 1$ m s^{-1} (———, magnesium; - - - -, cadmium; • • • • •, graphite/epoxy).

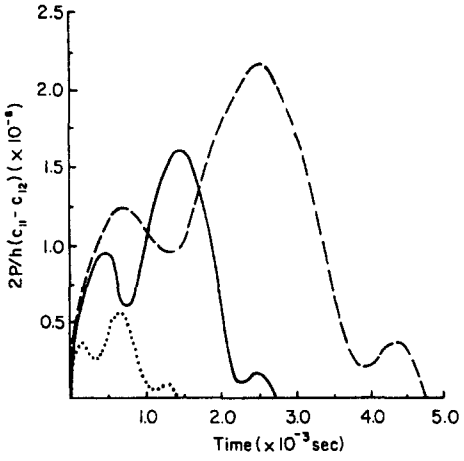

Fig. 2(b). Non-dimensionalized force history, simply supported beam, $V = 1$ m s^{-1}, $M = 0.5$ (———, magnesium; - - - -, cadmium; • • • • •, graphite/epoxy).

geometrical parameters used were the same as those in the isotropic study: $R = 40$ cm, $l = 10$ cm, and $h = 1$ cm. The mass densities of the materials are 1740 (magnesium), 8650 (cadmium), and 1384 kg m^{-3} (graphite/epoxy). It should be noted that, although the formulation of the equations in this section is such that they can be adapted to plane stress or plane strain, the use of beam theory equations in the superposition solution dictates that conditions of plane stress should be assumed in the evaluation of the constants K_{ij} in eqn (18). Furthermore, although a non-dimensional formulation would render the problem and its solution applicable to a wider variety of geometric configurations, the physical understanding for the relative magnitudes of forces, displacements, impact times, etc. in such a solution would be lost (see, e.g. Fig. 2(b) and compare with Fig. 2(a)). Hence, results were obtained in terms of real parameters. However, if a non-dimensional solution is desired, it may be obtained by solving eqn (39) after it has been put in dimensionless form using the following scheme:

$$\eta = x/h, \qquad \lambda = l/h, \qquad \alpha = R/h \tag{64a–c}$$

$$\sigma(t) = c(t)/h, \qquad y_n(\eta) = \sqrt{l}\, Y_n(x/h) \tag{64d, e}$$

Table 2. Scaling factors

Non-dimensional quantity	Multiply by
Contact length	h
Displacement	h
Pressure	$(c_{11}-c_{12})/2$
Force	$h(c_{11}-c_{12})/2$

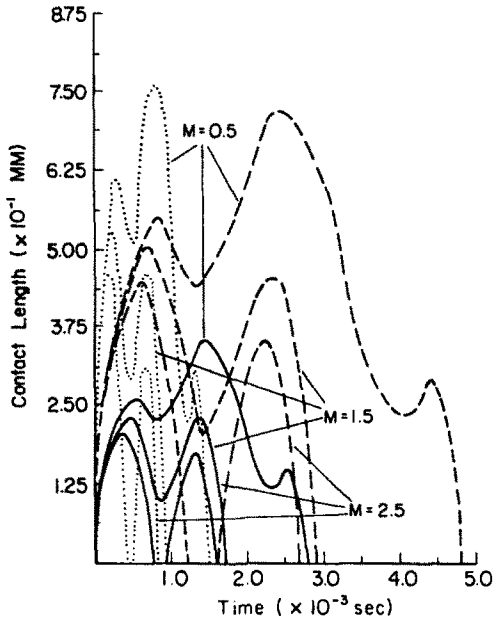

Fig. 3. Contact length history, simply supported beam, $V = 1$ m s^{-1} (———, magnesium; - - - -, cadmium; • • • • •, graphite/epoxy).

$$\pi(\eta, t) = 2p(x/h, t)/(c_{11}-c_{12}), \quad w_z(\eta, 0, t) = u_z(x/h, 0, t)/h. \tag{64f, g}$$

Non-dimensional curves and numbers can then be converted to real values by using the scaling factors given in Table 2.

The numerical results of this study are presented in the form of history curves and data comparison tables. The results for the simply supported beams are shown in Figs 2–7; those for the clamped beams are shown in Figs 8–10. Figures 2, 4 and 8 show contact force histories for the various impact velocities and mass ratios; Figs 3, 5 and 9 show contact length histories for the same impact velocities and mass ratios. Figures 6, 7 and 10 show typical contact pressure distributions. The peak normal stresses developed under the indenter for the various materials and end conditions are shown in Table 3; Tables 4 and 5 show a comparison between the numerical results and the values predicted by elementary beam theory for maximum transverse displacement and duration of impact.

From an examination of Figs 2–5, 8 and 9, when $M > 1.0$ (i.e. the beam is more massive than the projectile), the contact force and length histories are seen to have two peaks. This indicates that the beam is sufficiently flexible so that it achieves its maximum deflection after the contact area has reached its maximum value and has begun to diminish. After reaching its maximum deflection, the beam releases its stored energy and causes the projectile to reverse its trajectory. In this manner a new force maximum is achieved. For the largest value of the mass ratio, $M = 2.5$, in some cases the beam actually loses contact with the projectile and a second impact is observed (see, e.g. Fig. 7). However, there was no separation in those cases where a projectile was impacting a clamped beam. Clamped beams are not as flexible as simply supported ones and are thus less likely to give rise to double or multiple hit phenomena. This behavior is the same as that which was observed

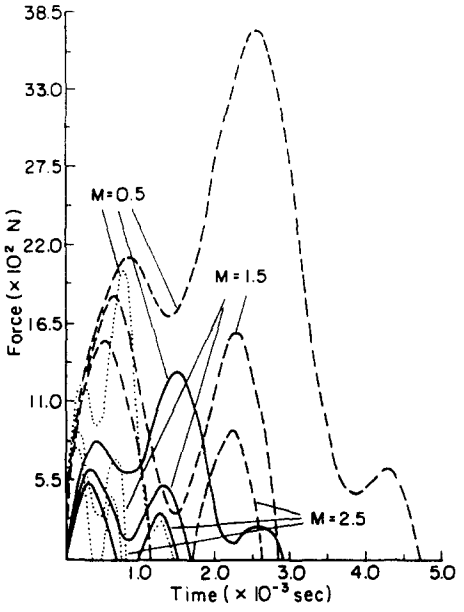

Fig. 4. Force history, simply supported beam, $V = 5$ m s^{-1} (———, magnesium; - - - - -, cadmium; • • • • •, graphite/epoxy).

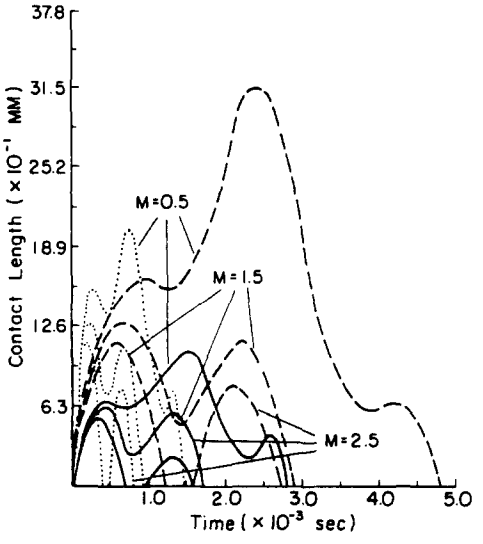

Fig. 5. Contact length history, simply supported beam, $V = 5$ m s^{-1} (———, magnesium; - - - - -, cadmium; • • • • •, graphite/epoxy).

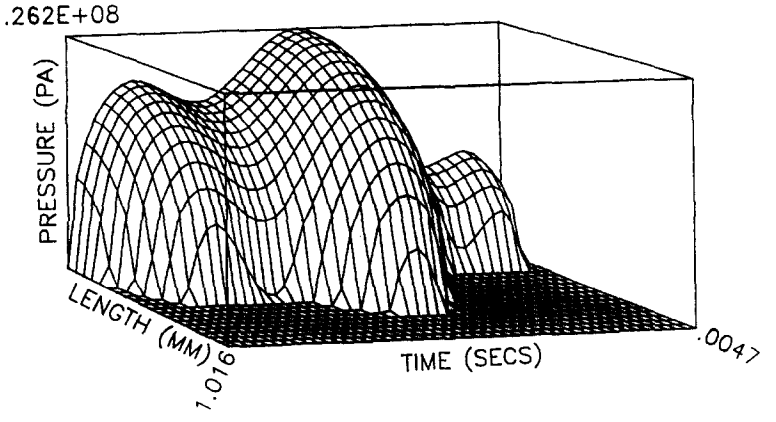

Fig. 6. Contact pressure distribution; simply supported cadmium beam, $M = 0.5$, $V = 1$ m s^{-1}.

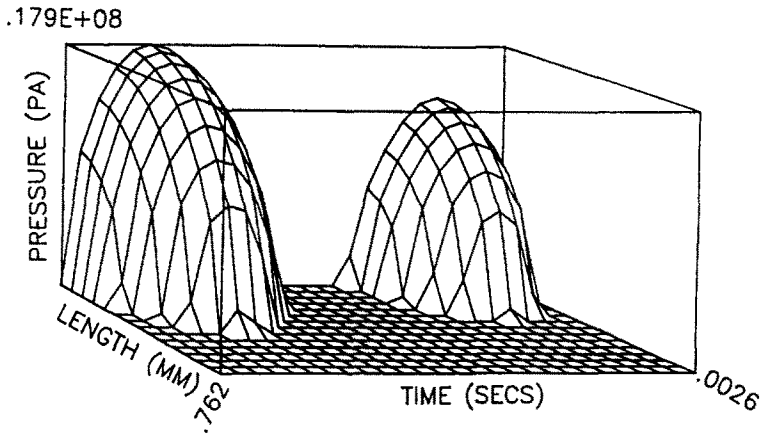

Fig. 7. Contact pressure distribution; simply supported cadmium beam, $M = 2.5$, $V = 1$ m s^{-1}.

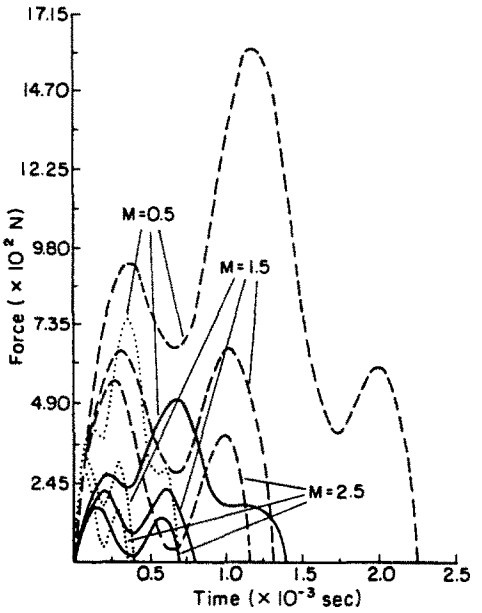

Fig. 8. Force history, clamped beam, $V = 1$ m s^{-1} (———, magnesium; - - - - -, cadmium; • • • • •, graphite/epoxy).

in the isotropic study[14] and in a recent study on the impact response of composite laminates[36]. In the cases where $M < 1.0$ the contact force and length histories are seen to have three peaks. This indicates that when the projectile is sufficiently more massive than the beam, it imparts enough energy to the beam so that the beam is able to impact the projectile twice: once after reaching maximum deflection, and once more during the rebound process. These figures also show that as M increases, the maximum force and contact length shift from the second peak to the first peak. This is because during rebound, when M is small, the lighter beam must transmit a much larger force to the heavier projectile in order to successfully reverse its trajectory. Moreover, peak contact forces and impact durations are found to increase as M decreases. This is in agreement with elementary beam theory predictions and the numerical results obtained in Ref. [36]. Furthermore, a comparison of the results obtained for different impact velocities reveals that the contact force and beam displacement histories for different impact velocities are similar in nature except for their respective amplitudes. The differences in the amplitudes are seen to be approximately proportional to the relative values of the initial impact velocities, which is again in agreement with the results obtained in Ref. [36]. Lastly the differences in behavior between clamped and simply supported beams are seen to be consistent with the predictions of elementary beam theory solutions (Tables 4 and 5).

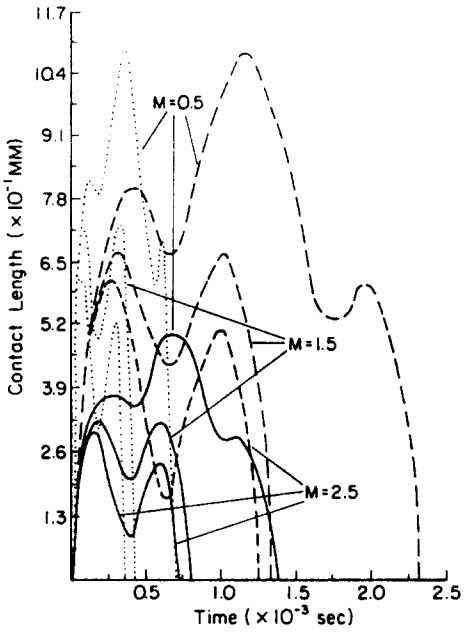

Fig. 9. Contact length history, clamped beam, $V = 1$ m s^{-1} (———, magnesium; - - - - -, cadmium; • • • • •, graphite/epoxy).

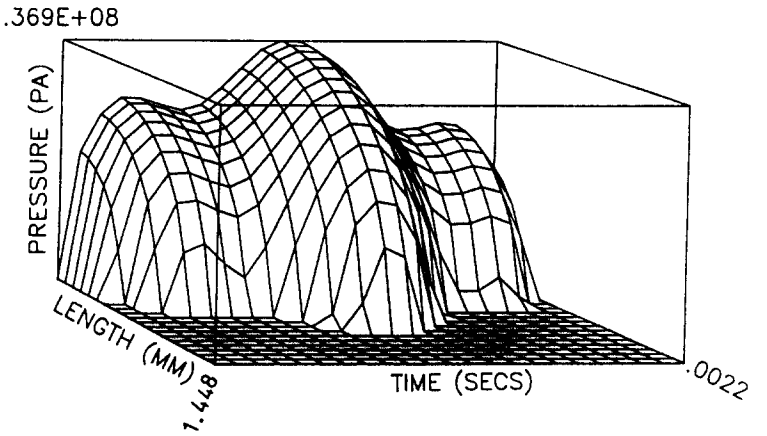

Fig. 10. Contact pressure distribution; clamped cadmium beam, $M = 0.5$, $V = 1$ m s^{-1}.

Table 3. Peak normal stress under the indenter—beam impact ($\times 10^7$ N m^{-2})

		Magnesium		Cadmium		Graphite/epoxy	
	M	Simply supported	Clamped	Simply supported	Clamped	Simply supported	Clamped
$V = 1$ m s^{-1}	0.5	1.843	2.603	2.620	3.690	1.315	1.787
	1.5	1.324	1.791	1.960	2.601	0.893	1.189
	2.5	1.194	1.687	1.789	2.401	0.836	1.121
$V = 5$ m s^{-1}	0.5	3.243	4.438	4.133	5.279	2.557	3.407
	1.5	2.649	3.687	3.770	5.015	1.895	2.639
	2.5	2.554	3.518	3.536	4.838	1.733	2.389

From an inspection of the results obtained in this study, it is seen that the effect of anisotropy on dynamic response is not as apparent as it was in the case of static indentation. Previously, it was shown[10–12] that the higher bending stiffness and lower transverse stiffness of beams made of highly anisotropic materials produce smaller transverse deflections, smaller contact forces, and larger contact lengths. As can be seen in Figs 2–5, 8 and 9 and Tables 3–5, this is not necessarily true in the case of dynamic impact. In Table 3,

Table 4. Maximum transverse displacement—beam impact (mm)

		Magnesium				Cadmium				Graphite/epoxy			
		Simply supported		Clamped		Simply supported		Clamped		Simply supported		Clamped	
	M	Elasticity	Beam theory	Elasticity	Beam theory	Elasticity	Beam theory	Elasticity	Beam theory	Elasticity	Beam theory	Elasticity	Beam theory
$V = 1\ \mathrm{m\ s^{-1}}$	0.5	0.765	0.498	0.386	0.254	1.311	0.848	0.678	0.434	0.399	0.246	0.208	0.127
	1.5	0.371	0.244	0.196	0.130	0.635	0.414	0.333	0.218	0.193	0.122	0.107	0.064
	2.5	0.269	0.168	0.140	0.089	0.457	0.284	0.236	0.152	0.139	0.084	0.079	0.043
$V = 5\ \mathrm{m\ s^{-1}}$	0.5	3.868	2.487	1.935	1.273	6.518	4.237	3.320	2.169	1.900	1.237	1.036	0.632
	1.5	1.842	1.219	0.973	0.643	3.167	2.073	1.664	1.092	0.965	0.605	0.538	0.320
	2.5	1.328	0.833	0.691	0.447	2.283	1.420	1.184	0.762	0.704	0.414	0.383	0.221

Table 5. Duration of impact—beam impact ($\times 10^{-2}$ s)

		Magnesium				Cadmium				Graphite/epoxy			
		Simply supported		Clamped		Simply supported		Clamped		Simply supported		Clamped	
	M	Elasticity	Beam theory	Elasticity	Beam theory	Elasticity	Beam theory	Elasticity	Beam theory	Elasticity	Beam theory	Elasticity	Beam theory
$V = 1\ \mathrm{m\ s^{-1}}$	0.5	0.270	0.194	0.130	0.095	0.470	0.331	0.220	0.162	0.140	0.096	0.068	0.047
	1.5	0.160	0.132	0.075	0.063	0.280	0.225	0.130	0.107	0.080	0.066	0.040	0.031
	2.5	0.150	0.116	0.065	0.054	0.260	0.197	0.110	0.092	0.075	0.058	0.036	0.027
$V = 5\ \mathrm{m\ s^{-1}}$	0.5	0.270	0.194	0.130	0.095	0.470	0.331	0.220	0.162	0.140	0.096	0.068	0.047
	1.5	0.160	0.132	0.075	0.063	0.280	0.225	0.130	0.107	0.080	0.066	0.040	0.031
	2.5	0.150	0.116	0.065	0.054	0.260	0.197	0.110	0.092	0.075	0.058	0.036	0.027

Table 6. Contact length rates of expansion—beam impact (m s^{-1})

	Simply supported	Clamped	c_0^*
Magnesium	1.3	3.1	3000
Cadmium	2.6	6.1	2000
Graphite/epoxy	6.1	15.2	7150

peak contact stresses of cadmium beams are in fact *greater* than those of the less anisotropic magnesium beams, whereas those of the highly anisotropic graphite/epoxy beams are indeed less than those of the cadmium and magnesium beams. Similarly, in Tables 4 and 5 it is seen that the maximum displacements and impact times experienced by cadmium beams are actually *larger* and *longer* than those experienced by corresponding magnesium beams, while the maximum displacements and impact times of graphite/epoxy beams are as expected. Tables 4 and 5 also show that these response characteristics are in agreement with the predictions of elementary beam theory. Examination of the beam theory equations reveals that the maximum transverse displacement and duration of impact are directly proportional to the square root of the mass of the beam, but inversely proportional to the square root of its bending stiffness. Thus, while the higher bending stiffness of cadmium beams should reduce deflections and impact times by approximately 25% as compared to corresponding magnesium beams, the higher mass density of the cadmium beams will *increase* deflections and impact times nearly 125% resulting in a net increase of almost 70% over magnesium beams. On the other hand, while graphite/epoxy beams are stiffer than magnesium beams, they are also lighter. This will result in a reduction of deflections and impact times of graphite/epoxy beams by nearly 50% over corresponding magnesium beams. Similar arguments can be used to explain the differences in the peak contact stresses as shown in Table 3. The relative sizes of the contact lengths of cadmium and magnesium beams, however, do agree with those predicted by the static indentation studies. The cadmium beams are less stiff in the transverse direction than corresponding magnesium beams (note the relative values of c_{33} in Table 1). As such, impacting projectiles penetrate more deeply into cadmium beams than magnesium beams which results in larger contact lengths for the cadmium beams. This argument, however, cannot be extended to the graphite/epoxy beams. Although graphite/epoxy beams are transversely softer than cadmium beams, the highly fibrous nature of graphite/epoxy prevents too much penetration from occurring. The stiffening effect of the fibers tends to cancel the effect of the transverse softness. This results in the peculiar contact length histories of the graphite/epoxy beams shown in Figs 3, 5 and 9.

A check of the quasi-static nature of the problem and solution was made by calculating average maximum rates of expansion of contact areas and comparing them with a characteristic wave speed of the materials as defined in Ref. [37]

$$c_0^* = \sqrt{((c_{11} - c_{12})/2\rho)}. \tag{65}$$

The results are presented in Table 6. It can be seen that the contact lengths expand much more slowly than the speed with which waves propagate through the beams. In view of these figures, the assumption of quasi-static response appears to be quite reasonable.

3. SECTION II: DYNAMIC IMPACT OF A CIRCULAR PLATE

3.1. *Introduction*

In this section we examine the low velocity impact of a rigid projectile on an elastically supported transversely isotropic circular plate. The assumptions and simplifications used in the previous section (i.e. local deformation is elastic and occurs quasistatically, elastodynamic effects are neglected, etc.) are assumed to be valid for problems of plate impact as well[38].

The solution to the dynamic contact problem at hand is obtained as a superposition of a static axisymmetric solution similar to the one developed by Keer and Miller[13] with a dynamic plate theory solution[19]. Application of appropriate boundary conditions leads to a Volterra integral equation that is again solved numerically. To assess the effects of anisotropy on the plate's response, solutions are obtained for plates made of magnesium and cadmium.

It is again noted that because the impact velocity is low, the approximations of elementary plate theory are valid and should yield accurate results[39]. If the impact velocity were high or the duration of contact very short, then corrections for shear and rotary inertia would have to be incorporated into the analysis[40].

3.2. *Problem formulation*

3.2.1. *Static axisymmetric solution.* The boundary conditions for the layer solution are those of an elastically supported axisymmetric layer of thickness h loaded on the upper surface by a smooth axisymmetric rigid indenter

$$\tau_{zz}(r,h) = 0, \qquad 0 < r < \infty \tag{1}$$

$$\tau_{rz}(r,h) = 0, \qquad 0 < r < \infty \tag{2}$$

$$\tau_{rz}(r,0) = 0, \qquad 0 < r < \infty \tag{3}$$

$$\tau_{zz}(r,0) = 0, \qquad c < r < \infty \tag{4}$$

$$\tau_{zz}(r,0) = -p(r), \qquad 0 < r < \infty \tag{5}$$

where c is the radius of the area of contact. The static plate boundary conditions are given by

$$u_z = 0, \qquad M_r - K\bar{\theta}_r = 0, \qquad r = a \tag{6,7}$$

where a is the radius of the plate.

The elasticity solution that represents loading on the upper surface of an axisymmetric transversely isotropic layer and no loading on the lower surface is obtained by applying the technique used in Section I to axisymmetric materials (see, e.g. England[41]) and is given by

$$\tau_{zz} = \int_0^\infty E(\xi)K_1(\xi)\xi J_0(\xi r)\,d\xi, \qquad \tau_{rz} = -\int_0^\infty E(\xi)K_2(\xi)\xi J_1(\xi r)\,d\xi \tag{8,9}$$

$$\tau_{rr} = \int_0^\infty E(\xi)\left[K_3(\xi)\xi J_0(\xi r) + \frac{c_{11}-c_{12}}{c_{44}r}K_5(\xi)J_1(\xi r)\right]d\xi \tag{10}$$

$$u_z = \frac{1}{c_{44}}\int_0^\infty E(\xi)K_4(\xi)J_0(\xi r)\,d\xi, \quad u_r = -\frac{1}{c_{44}}\int_0^\infty E(\xi)K_5(\xi)J_1(\xi r)\,d\xi \tag{11,12}$$

where the kernels $K_1(\xi)$ through $K_5(\xi)$ are identical to those in Section I, eqns (9)–(13), respectively. The normal and shear stress vanish automatically on $z = h$ as does the shear stress on $z = 0$. The normal stress on $z = 0$ is given as

$$\tau_{zz}(r,0) = \int_0^\infty \xi E(\xi)J_0(\xi r)\,d\xi. \tag{13}$$

Substituting eqn (13) into eqns (4) and (5) and taking a Hankel transform yields

$$E(\xi) = -\int_0^c rp(r)J_0(\xi r)\,dr. \tag{14}$$

The moment and average slope due to this layer solution are given by

$$M_E = -\int_0^\infty \xi^{-2}E(\xi)\left[\xi J_0(\xi r) - \frac{c_{11}-c_{12}}{c_{44}r}\frac{B(\xi)}{D(\xi)}J_1(\xi r)\right]d\xi \tag{15}$$

$$\bar{\theta}_E = \frac{\sqrt{\nu_2}}{c_{44}}\int_0^\infty \frac{E(\xi)F(\xi)}{D(\xi)}J_1(\xi r)\,d\xi \tag{16}$$

where

$$B(\xi) = \sqrt{\nu_2}\left(\frac{\nu_1}{1+\kappa_1}+\frac{\nu_2}{1+\kappa_2}\right)(\operatorname{ch}\beta_1\operatorname{ch}\beta_2-1) - \frac{1}{\sqrt{\nu_1}}\left(\frac{\nu_1^2}{1+\kappa_1}+\frac{\nu_2^2}{1+\kappa_2}\right)\operatorname{sh}\beta_1\operatorname{sh}\beta_2$$
$$+\left(\frac{\nu_1}{1+\kappa_1}-\frac{\nu_2}{1+\kappa_2}\right)\left[\sqrt{\nu_2}(\operatorname{ch}\beta_1-\operatorname{ch}\beta_2)-\xi h\left(\sqrt{\left(\frac{\nu_2}{\nu_1}\right)}\operatorname{sh}\beta_1-\operatorname{sh}\beta_2\right)\right] \tag{17}$$

and $F(\xi)$ is as defined in Section I, eqn (23).

The static plate theory solution is taken in the form of a quadratic displacement solution given by

$$u_z(r) = \frac{1}{2}Ar^2 + B \tag{18}$$

which results in a moment and average slope given by

$$M_p = -D_p^* A, \qquad \bar{\theta}_p = Ar \tag{19,20}$$

where $D_p^* = h^3(c_{11}+c_{12}-2c_{13}^2/c_{33})/12$. The constants A and B are obtained by applying the plate boundary conditions to appropriately superposed plate theory and elasticity expressions. The resulting values are

$$A = -\frac{1}{D_p^*(1+\alpha_p^*)}\int_0^\infty E(\xi)\left[\frac{J_0(\xi a)}{\xi} - \frac{c_{11}-c_{12}}{c_{44}a}\frac{B(\xi)}{D(\xi)}\frac{J_1(\xi a)}{\xi^2} + \frac{D_p^*\alpha_p^*\sqrt{\nu_2}}{c_{44}ah}\frac{F(\xi)}{D(\xi)}J_1(\xi a)\right]d\xi \tag{21}$$

$$B = \frac{1}{D_p^*}\int_0^\infty E(\xi)\left[\frac{a^2}{2(1+\alpha_p^*)}\frac{J_0(\xi a)}{\xi} - \frac{c_{11}-c_{12}}{c_{44}a}\frac{B(\xi)}{D(\xi)}\frac{J_1(\xi a)}{\xi^2}\right.$$
$$\left.+\frac{D_p^*\sqrt{\nu_2}a}{2c_{44}h}\frac{\alpha_p^*}{1+\alpha_p^*}\frac{F(\xi)}{D(\xi)}J_1(\xi a) + \frac{D_p^*}{c_{44}}\left(\frac{\kappa_1}{1+\kappa_1}-\frac{\kappa_2}{1+\kappa_2}\right)\frac{G(\xi)}{D(\xi)}J_0(\xi a)\right]d\xi \tag{22}$$

where $\alpha_p^* = Ka/D_p^*$ and $G(\xi)$ is given by Section I, eqn (15). Following the same procedure as in Section I, the total transverse deflection is given by

$$u_z(r,0) = \int_0^c r'L(r,r')p(r')\,dr' + \frac{1}{2D_p^*}\int_0^c r'K(r,r')p(r')\,dr' \tag{23}$$

where

$$L(r,r') = \frac{2}{\pi}\delta_1\left[\frac{H(r-r')}{r}K\left(\frac{r'}{r}\right) + \frac{H(r'-r)}{r'}K\left(\frac{r}{r'}\right) - \frac{1}{a}K\left(\frac{r'}{a}\right)\right] - \frac{a^2-r^2}{2a^2h}\frac{\alpha_p^*}{1+\alpha_p^*}\delta_2 \quad (24)$$

$$K(r,r') = \int_0^\infty J_0(\xi r')\left\{\frac{2D_p^*}{c_{44}}\left(\frac{\kappa_1}{1+\kappa_1} - \frac{\kappa_2}{1+\kappa_2}\right)\left[\frac{G(\xi)}{D(\xi)} - \frac{1}{\sqrt{\nu_1}-\sqrt{\nu_2}}\right][J_0(\xi r)-J_0(\xi a)]\right.$$
$$\left. - \frac{a^2-r^2}{1+\alpha_p^*}\left(\frac{J_0(\xi a)}{\xi} - \frac{c_{11}-c_{12}}{c_{44}a}\frac{B(\xi)}{D(\xi)}\frac{J_1(\xi a)}{\xi^2} + \frac{\alpha_p^* D_p^*}{ah}\left[\frac{\sqrt{\nu_2}}{c_{44}}\frac{F(\xi)}{D(\xi)} - \delta_2\right]J_1(\xi a)\right)\right\}d\xi \quad (25)$$

and δ_1, δ_2 are given by Section I, eqns (31) and (32). The functions $K(p)$ are complete elliptic integrals of the first kind.

3.2.2. *Dynamic plate theory solution.* Using a Laplace transform technique and a normal mode expansion, the deflection of an axisymmetric circular plate initially at rest is given by

$$u_z(r,t) = \frac{1}{\rho h}\sum_{n=1}^{\infty}\frac{Y_n(r)}{\omega_n^*}\int_0^a r' Y_n(r')\int_0^t p(r',\tau)\sin[\omega_n^*(t-\tau)]\,d\tau\,dr' \quad (26)$$

where $\omega_n^* = \beta_n^2\sqrt{(D_0^*/\rho h)}$, and $D_0^* = h^3(c_{11}-c_{13}^2/c_{33})/12$. The normal modes Y_n are defined by

$$Y_n(r) = A_n\left[J_0(\beta_n r) - \frac{J_0(\beta_n a)}{I_0(\beta_n a)}I_0(\beta_n r)\right]. \quad (27)$$

The coefficients A_n and frequency equations that yield the β_n for the edge conditions considered in subsequent numerical calculations are given as follows:

simply supported edge

$$2\beta_n a I_0(\beta_n a)J_0(\beta_n a) - \left(\frac{c_{11}-c_{12}}{c_{11}-c_{13}^2/c_{33}}\right)[I_0(\beta_n a)J_1(\beta_n a)+I_1(\beta_n a)J_0(\beta_n a)] = 0$$

$$\frac{1}{A_n^2} = a^2\left\{J_0^2(\beta_n a)+J_1^2(\beta_n a) - \left[J_0(\beta_n a)\frac{I_1(\beta_n a)}{I_0(\beta_n a)} + J_1(\beta_n a)\right]\right.$$
$$\left.\times\left[\frac{1}{\beta_n a}J_0(\beta_n a) - \frac{1}{2}\left(J_0(\beta_n a)\frac{I_1(\beta_n a)}{I_0(\beta_n a)} - J_1(\beta_n a)\right)\right]\right\};$$

clamped edge

$$I_0(\beta_n a)J_1(\beta_n a)+I_1(\beta_n a)J_0(\beta_n a) = 0, \qquad \frac{1}{A_n^2} = a^2[J_0^2(\beta_n a)+J_1^2(\beta_n a)].$$

3.2.3. *Superposition solution—integral equation for the dynamic problem.* Superposing the static and dynamic expressions for $u_z(r,t)$ yields

$$u_z(r,0,t) = \int_0^{c(t)} r'L(r,r')p(r')\,dr' + \frac{1}{2D_p^*}\int_0^{c(t)} r'K(r,r')p(r')\,dr' + \frac{1}{\rho h}\int_0^t\int_0^{c(\tau)} r'p(r',\tau)\sum_{n=1}^{\infty}\frac{Y_n(r)Y_n(r')}{\omega_n^*}\sin[\omega_n^*(t-\tau)]\,dr'\,d\tau. \quad (28)$$

In the contact region the governing equations are

$$u_z(r,0,t) = \Delta(t) - r^2/2R \quad (29)$$

$$\Delta(t) = Vt - \frac{2M}{\rho a^2 h}\int_0^t (t-\tau)\int_0^{c(\tau)} r'p(r',\tau)\,dr'\,d\tau. \quad (30)$$

As before, R is the radius of curvature of the projectile, M is the ratio of the mass of the plate to that of the projectile, and V is the initial impact velocity. Substituting eqns (29) and (30) into eqn (28) yields the integral equation for the impact problem

$$\int_0^{c(t)} r'L(r,r')p(r',t)\,dr' + \frac{1}{2D_p^*}\int_0^{c(t)} r'K(r,r')p(r',t)\,dr' + \frac{1}{\rho h}\int_0^t\int_0^{c(\tau)} r'p(r',\tau)M(r,r',\tau)\,dr'\,d\tau + \frac{2M}{\rho a^2 h}\int_0^t (t-\tau)\int_0^{c(\tau)} r'p(r',\tau)\,dr'\,d\tau = Vt - r^2/2R \quad (31)$$

where $M(r,r'\tau)$ is given by

$$M(r,r',\tau) = \sum_{n=1}^{\infty}\frac{Y_n(r)Y_n(r')}{\omega_n^*}\sin[\omega_n^*(t-\tau)]. \quad (32)$$

3.3. *Numerical solution*

In solving eqn (31) numerically, the same scheme is used as in the two-dimensional case. After performing the required manipulations, we have

$$\sum_{j=1}^{N_k} A_{ij}^{(k)} p_j^{(k)} = B_i^{(k)}, \qquad i = 1,2,\ldots,N_k \quad (33)$$

where

$$A_{ij}^{(k)} = S(r_i,r_j) + \frac{1}{\rho h}\sum_{n=1}^{\infty}\frac{Y_n(r_i)I_n(r_j)}{\omega_n^*}W_{kk}^{(n)} + \frac{2M}{\rho a^2 h}(\Delta r)r_j w_{kk}^{i} \quad (34)$$

$$B_{ij}^{(k)} = Vt_k - r_i^2/2R - \sum_{l=1}^{k-1}\left\{\sum_{j=1}^{N_l}\left[\frac{1}{\rho h}\sum_{n=1}^{\infty}\frac{Y_n(r_i)I_n(r_j)}{\omega_n^*}W_{kl}^{(n)} + \frac{2M}{\rho a^2 h}(\Delta r)r_j w_{kl}^{i}\right]p_j^{(l)}\right\} \quad (35)$$

$$S(r_i,r_j) = \int_{r_j-\Delta r/2}^{r_j+\Delta r/2}\left[L(r_i,r') + \frac{1}{2D_p^*}K(r_i,r')\right]r'\,dr' \quad (36)$$

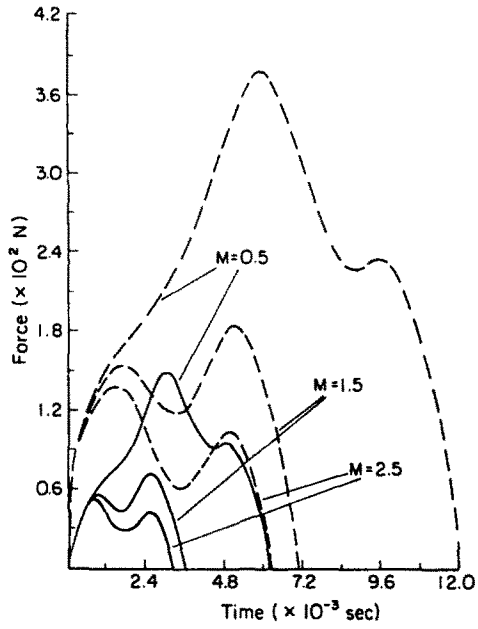

Fig. 11. Force history, simply supported plate, $V = 1$ m s^{-1} (———, magnesium; - - - -, cadmium).

$$I_n(r_j) = \int_{r_j-\Delta r/2}^{r_j+\Delta r/2} Y_n(r')r'\,dr' \tag{37}$$

3.4. *Elementary plate theory solutions*

The impact times and maximum transverse displacements obtained in the solution of eqn (33) are compared with those obtained using an elementary plate impact solution[42]. In this solution, the duration is found to be

$$t^0 = \pi\sqrt{(k/m_p - \beta^2 k^2/4)} \tag{38}$$

and the maximum displacement is given by

$$u^0_{z,\max} = Vm_p\beta\left(1 - \frac{\beta k t^0}{2\pi}e^{-\beta k t^0/4}\right) \tag{39}$$

where $\beta^2 = 1/64\rho h D_0^*$, m_p is the mass of the projectile, and k is the amount of static force required to produce a unit transverse displacement at the center of a circular plate. For the edge conditions considered in subsequent numerical calculations, k is given as follows:

$$\textit{simply supported edge} \qquad k = 16\pi(1+\nu^*)D_0^*/(3+\nu^*)a^2 \tag{40}$$

$$\textit{clamped edge} \qquad k = 16\pi D_0^*/a^2 \tag{41}$$

where

$$\nu^* = (c_{12} - c_{13}^2/c_{33})/(c_{11} - c_{13}^2/c_{33}).$$

3.5. *Observations and conclusions*

Two materials were used in the plate impact study: magnesium and cadmium. For each material, solutions were obtained for simply supported and clamped edge conditions, and for impact velocities of 1 and 3 m s^{-1}; the mass ratio M was varied from 0.5 to 2.5. In each case, the following geometrical parameters were used: $R = 40$ cm, $a = 10$ cm, and $h = 0.25$ cm. As in the two-dimensional study, equations were solved and results were obtained in terms of real parameters. If a non-dimensional solution is desired, it may be obtained by solving eqn (31) after it has been nondimensionalized using a scheme similar to that given in Section I. Real values may then be obtained from dimensionless curves and numbers using Table 2, with h^2 replacing h in the force scaling factor.

The numerical results are presented in the form of history curves and data comparison tables. Figures 11 and 12 show contact force and radius histories for various mass ratios;

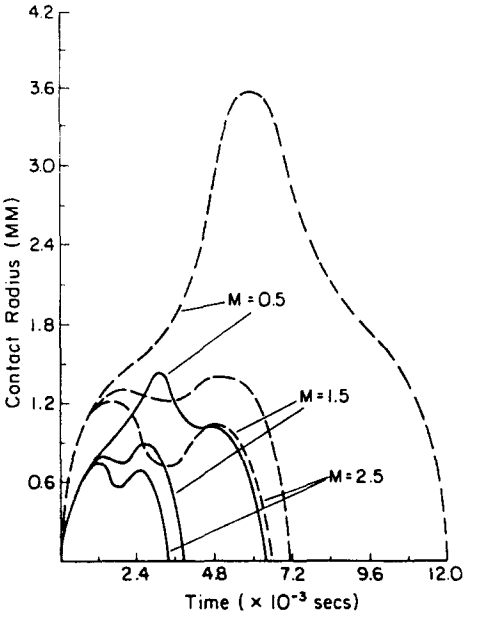

Fig. 12. Contact radius history, simply supported plate, $V = 1$ m s^{-1} (———, magnesium; - - - - -, cadmium).

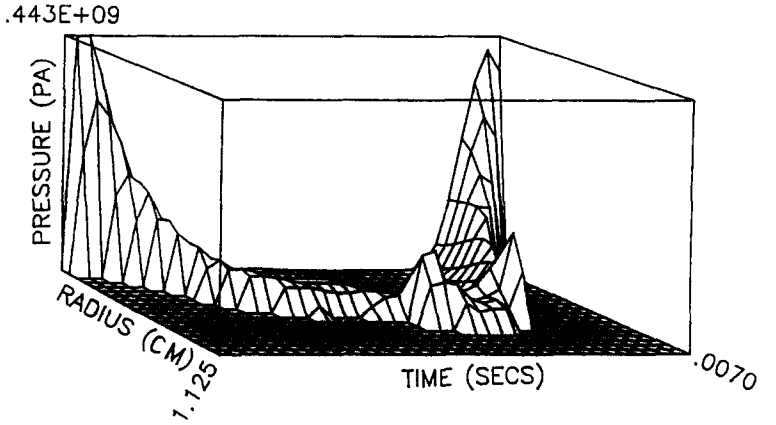

Fig. 13. Contact pressure distribution; simply supported cadmium plate, $M = 1.5$, $V = 3$ m s^{-1}.

Table 7. Maximum transverse displacement—plate impact (mm)

		Magnesium				Cadmium			
		Simply supported		Clamped		Simply supported		Clamped	
	M	Elasticity	Plate theory	Elasticity	Plate theory	Elasticity	Plate theory	Elasticity	Plate theory
$V = 1$ m s^{-1}	0.5	2.044	1.583	1.129	†	3.886	2.817	2.036	†
	1.5	1.109	0.519	0.628	0.517	2.091	0.943	1.115	0.933
	2.5	0.796	0.321	0.465	0.307	1.507	0.584	0.839	0.554
$V = 3$ m s^{-1}	0.5	—	4.749	—	†	—	8.450	—	†
	1.5	3.018	1.558	1.882	1.551	6.264	2.830	3.362	2.799
	2.5	2.102	0.964	1.393	0.921	4.513	1.753	2.502	1.662

Fig. 13 shows an extreme case of a contact pressure distribution. Tables 7 and 8 show a comparison between the numerical results and the values predicted by elementary plate theory equations for maximum transverse displacement and duration of impact.

The results obtained in this section are similar to those obtained in the beam impact study concerning the effect of impact velocity, mass ratio, edge support, anisotropy, etc. on displacements, impact times, contact areas and forces. There are, however, several notable differences.

Table 8. Duration of impact—plate impact ($\times 10^{-2}$ s)

	Magnesium				Cadmium			
	Simply supported		Clamped		Simply supported		Clamped	
M	Elasticity	Plate theory	Elasticity	Plate theory	Elasticity	Plate theory	Elasticity	Plate theory
0.5	0.620	0.628	0.340	†	1.200	1.142	0.620	†
1.5	0.360	0.282	0.200	0.213	0.700	0.533	0.360	0.384
2.5	0.320	0.210	0.170	0.146	0.620	0.400	0.310	0.263

Table 9. Contact area rates of expansion—plate impact (m s^{-1})

	Simply supported	Clamped	c_0^*
Magnesium	7.0	12.0	3000
Cadmium	7.5	15.0	2000

Table 10. Calculated (Schonberg), predicted (Shivakumar), and measured (Lal) impact forces and durations

	Velocity (m s^{-1})	Schonberg	Shivakumar	Lal
Impact force (kN)	1.0	0.122	0.115	0.104†
	3.0	0.367	0.463	0.512†
	5.0	0.614	0.920	1.274†
Impact duration (s)	1.0	0.00170	0.00215	0.00196†
	3.0	0.00170	0.00173	0.00170†
	5.0	0.00170	0.00144	0.00152†

First, there was no loss of contact between the projectile and the plate. This indicates that even thin, simply supported plates are sufficiently stiff so as not to give rise to a double-hit phenomenon. Second, in cases where the impact velocity was high or the mass ratio large, the resulting pressure distributions were highly non-Hertzian, a characteristic not seen in the two-dimensional study (see, e.g. Fig. 13). Third, when $M < 1$ it was observed that the force and contact radius histories exhibited only two peaks, not three as in the two-dimensional study. This indicates a more gradual build-up of stresses within the plate and a slower release rate after the force maximum is obtained. As M increases the force and contact radius history curves begin to resemble the curves obtained in the beam impact study. It should be noted that the entries marked "†" in Tables 7 and 8 indicate that the elementary plate theory solution predicts that in those cases the projectile will not rebound. Since the plate theory predictions were derived using a linear spring constant, it is understandable that, in several of those cases, the full elasticity solution shows that rebound will indeed occur. The entries marked "—" in Tables 7 and 8 indicate that the numerical scheme is unstable in these particular cases.

Average maximum rates of expansion of the contact areas are given in Table 9. A comparison of these figures with the characteristic wave speeds for the plate materials reveals that the contact areas expand much more slowly than the speed with which waves propagate through the plate. This again confirms the quasi-static nature of the problem and its solution.

As a test of the validity of the solution technique presented in this section (and the previous section as well), solutions were obtained using parameters of previous theoretical and experimental studies of low velocity impact on circular plates (Ref. [43] and Ref. [44], respectively). Numerical results for impact velocities of 1, 3 and 5 m s^{-1} are given in Table 10 (a number with a dagger next to it indicates an interpolated value). It is seen that the elasticity solution developed in this paper agrees well with previous analytical and experimental results for impact duration, but differs with the results for maximum impact

force, especially at higher velocities. These discrepancies are probably due to several major assumptions implicit in the solution developed here. First, the impact phenomenon is assumed to occur elastically. Previous experimental studies have shown that composite plates usually experience some plastic deformation near the site of impact[45]. Second, small deformation theory is assumed valid in the construction of the static part of the solution, Sections 2.2.1 and 3.2.1. However, laminated plates have been found to undergo large deformations and membrane stretching even when the impact occurs at low velocity[44, 46]. Lastly, inertial effects have been neglected in the construction of the static elasticity layer solution. Inclusion of such effects can be expected to alter peak forces as well as durations of impact.

4. SUMMARY

The low velocity impact problems of a rigid smooth projectile striking elastically supported transversely isotropic beams and plates are solved. The results obtained indicate that the mass of the beam or plate significantly affects the dynamic response of the member. While separation and double-hits occurred often in the two-dimensional impact study, it was found that the increased stiffness of the three-dimensional problem prevented such phenomena from occurring. In general, impact force, maximum transverse displacement, and duration of impact were found to be directly proportional to the beam or plate mass, and inversely proportional to the bending stiffness of the member. Contact area was found to be inversely proportional to the transverse stiffness of the member. It should be noted that inhomogeneous materials require special attention and that caution should be employed in extending these conclusions to such materials. Finally, the solutions developed here were found to yield results that agreed reasonably well with previous experimental test data.

Acknowledgement—The authors are grateful for support from the Air Force Office of Scientific Research under Grant AFOSR-82-0330.

REFERENCES

1. J. M. Kelly, The impact of a mass on a beam. *Int. J. Solids Structures* **3,** 191 (1967).
2. J. E. Beneviste, Sonic boom effects on beams loosely bound to their supports. *J. Aircraft* **4**(6), 494 (1967).
3. G. N. Bycroft, Impact of a rigid body on an elastic half-space. *J. Appl. Mech.* **44**(4), 227 (1977).
4. D. A. Hills, Some aspects of post yield contact problems. *Wear* **85,** 107 (1983).
5. C. T. Sun, An analytical method for evaluation of impact damage energy of laminated composites. 4th Conf. Comp. Mat. Test. Design, ASTM STP 617, p. 427 (1977).
6. I. M. Hutchings, R. E. Winter and J. E. Field, Solid particle erosion of metals: the removal of surface material by spherical projectiles. *Proc. R. Soc. Lond.* **A348,** 379 (1976).
7. I. M. Hutchings, Deformation of metal surface by the oblique impact of square plates. *Int. J. Mech. Sci.* **9,** 45 (1977).
8. J. F. Doyle, An experimental method for determining the dynamic contact law. *Expl Mech.* **24,** 10 (1984).
9. L. M. Keer and G. R. Miller, Smooth indentation of a finite layer. *J. Engng Mech. Div. ASCE* **109,** 706 (1983).
10. L. M. Keer and R. Ballarini, Smooth contact between a rigid indenter and an initially stressed orthotropic beam. *AIAA J.* **21,** 1035 (1983).
11. L. M. Keer and W. P. Schonberg, Smooth indentation of an isotropic cantilever beam. *Int. J. Solids Structures* **22,** 87 (1986).
12. L. M. Keer and W. P. Schonberg, Smooth indentation of a transversely isotropic cantilever beam. *Int. J. Solids Structures* **22,** 1033 (1986).
13. L. M. Keer and G. R. Miller, Contact between an elastically supported circular plate and a rigid indenter. *Int. J. Engng Sci.* **21,** 681 (1983).
14. L. M. Keer and J. C. Lee, Dynamic impact of an elastically supported beam—large area contact. *Int. J. Engng Sci.* **23,** 987 (1985).
15. D. Tabor, *The Hardness of Metals*, p. 130. Oxford University Press, Oxford (1950).
16. C. T. Sun and S. N. Huang, Transverse impact problems by higher order beam finite element. *Comput. Struct.* **5,** 297 (1975).
17. Y. M. Tsai and H. Kolsky, A study of the fractures produced in glass blocks by impact. *J. Mech. Phys. Solids* **15,** 263 (1967).
18. W. Goldsmith, T. W. Liu and S. Chulay, Plate impact and perforation. *Expl Mech.* **5,** 385 (1965).
19. K. F. Graff, *Wave Motion in Elastic Solids*. Ohio State University Press, Columbus, Ohio (1975).
20. C. T. H. Baker, *The Numerical Treatment of Integral Equations*, Oxford University Press, London (1977).
21. N. Ahmadi, L. M. Keer and T. Mura, Non-Hertzian contact stress analysis for an elastic half-space—normal and sliding contact. *Int. J. Solids Structures* **19,** 357 (1983).

22. N. J. Pagano, Exact moduli of anisotropic laminates. In *Mechanics of Composite Materials* (Edited by G. P. Sendeckyi), Vol. 2. Academic Press, New York (1974).
23. J. E. Beneviste, Comparison of beam impact models. *AIAA J.* **8**(4), 823 (1970).
24. C. C. Fu, Closed-form solutions of an infinite beam under impact loading. *Int. J. Solids Structures* **3**, 607 (1967).
25. C. V. Raman, On some applications of Hertz's theory of impact. *Phys. Rev.* **15**(4), 277 (1920).
26. S. C. Hunter, Energy absorbed by elastic waves during impact. *J. Mech. Phys. Solids* **5**, 162 (1957).
27. Y. M. Tsai, Dynamic stresses produced by the impact of an axisymmetrical projectile on an elastic half-space. *Int. J. Solids Structures* **7**, 543 (1971).
28. W. H. Hoppmann, Impact of a mass on a damped elastically supported beam. *J. Appl. Mech.* **15**, 125 (1948).
29. D. G. Christopherson, Effect of shear in transverse impact on beams. *Proc. Instn Mech. Engrs* **165**(WEP67), 176–188 (1951).
30. M. Goland and M. A. Dengler, Transverse impact of long beams, including rotary inertia and shear effects. In *Proc. 1st US Nat. Congr. Appl. Mech.*, pp. 179–186 (1952).
31. M. Goland, P. D. Wickersham and M. A. Dengler, Propagation of elastic impact in beams in bending. *ASME J. Appl. Mech.* **22**(1), 1 (1955).
32. B. A. Boley, An approximate theory of lateral impact on beams. *ASME J. Appl. Mech.* **22**(1), 69 (1955).
33. A. E. Green and W. Zerna, *Theoretical Elasticity*. Oxford University Press, London (1954).
34. I. N. Sneddon, *Fourier Transforms*. McGraw-Hill, New York (1951).
35. W. Goldsmith, *Impact: The Theory and Physical Behavior of Colliding Solids*. Edward Arnold, London (1960).
36. C. T. Sun and J. K. Chen, On the impact of initially stressed composite laminates. *J. Comp. Mat.* **19**, 490 (1985).
37. M. J. P. Musgrave, On the propagation of elastic waves in aeolotropic media II: media of hexagonal symmetry. *Proc. R. Soc.* **A226**, 356 (1954).
38. J. C. S. Yang, Impact on plates and shells. *Int. J. Solids Structures* **7**, 445 (1971).
39. J. P. A. Tillett, A study of the impact of spheres on plates. *Proc. Phys. Soc.* **B67**, 677 (1954).
40. R. D. Mindlin, Influence of rotary inertia and shear on flexural motions of isotropic elastic plates. *J. Appl. Mech.* **18**(1), 31 (1951).
41. A. H. England, A punch problem for a transversely isotropic layer. *Proc. Camb. Phil. Soc.* **58**, 539 (1962).
42. H. D. Conway and H. C. Lee, Impact of an indenter on a large plate. *J. Appl. Mech.* **37**(1), 234 (1970).
43. K. N. Shivakumar, W. Elber and W. Illg, Prediction of impact force and duration due to low-velocity impact on circular composite laminates. *J. Appl. Mech.* **52**(3), 674 (1985).
44. K. M. Lal, Prediction of residual tensile strength of transversely impacted composite laminates. In *Research in Structural and Solids Mechanics* (Edited by J. M. Housner and A. K. Noor), NASA CP 2245 (1982).
45. L. B. Greszczuk, Damage in composite materials due to low velocity impact. In *Impact Dynamics* (Edited by J. A. Zukas *et al.*), Wiley, New York (1982).
46. W. Elber, Failure mechanics of low velocity impacts on thin composite plates. NASA TP 2152 (May 1983).

APPENDIX: INTEGRATION WEIGHTS

The weights w_{kl}^c, w_{kl}^s and w_{kl}^i are calculated by spanning the time domain with a series of Lagrange interpolation polynomials. Their exact values depend on whether the current time-step is even or odd.

Even time-step: $t_k = k(\Delta t)$, $k = 2m$, $m \geqslant 1$

If the time-step is even, then Filon's formula is used to evaluate the integrals involving $f_n(t)$ in eqn (46). The weights w_{kl}^c, w_{kl}^s can be found in any standard handbook on numerical analysis. The weights w_{kl}^i are calculated by spanning the intervals of the time domain with a series of quadratic interpolation polynomials, two intervals per polynomial. Performing the indicated integrations yields

$$w_{kl}^i = \begin{cases} 4(\Delta t)^2(k-l)/3 \ldots l \text{ odd} \\ 2(\Delta t)^2(k-l)/3 \ldots l \text{ even.} \end{cases} \tag{A1}$$

Odd time-step: $t_k = k(\Delta t)$, $k = 2m+1$, $m \geqslant 1$

If the time-step is odd, then a modified version of Filon's formula is used to evaluate the integrals involving $f_n(t)$. Consider one of these integrals rewritten as follows:

$$\int_0^{t_k} f_n(\tau)\cos(\omega_n^*\tau)\,d\tau = \int_0^{t_{k-3}} f_n(\tau)\cos(\omega_n^*\tau)\,d\tau + \int_{t_{k-3}}^{t_k} f_n(\tau)\cos(\omega_n^*\tau)\,d\tau. \tag{A2}$$

Since t_{k-3} is an even time-step, Filon's formula is used to evaluate the first integral on the right-hand side of eqn (A2). The second integral is evaluated by spanning the last three intervals of time with a cubic interpolation polynomial. Performing the required integration, eqn (A2) can be written as

$$\int_0^{t_k} f_n(\tau)\cos(\omega_n^*\tau)\,d\tau = \sum_{l=1}^{k} w_{kl}^c f_l \tag{A3}$$

where

$$w_{kl}^{c} = \begin{cases} w_{k-3,l}^{c} & \ldots 1 \leqslant l \leqslant k-4 \\ w_{k-3,k-3}^{c} - I_{cc}(t_{k-2}, t_{k-1}, t_k)/6(\Delta t)^3 & \ldots l = k-3 \\ I_{cc}(t_{k-3}, t_{k-1}, t_k)/2(\Delta t)^3 & \ldots l = k-2 \\ -I_{cc}(t_{k-3}, t_{k-2}, t_k)/2(\Delta t)^3 & \ldots l = k-1 \\ I_{cc}(t_{k-3}, t_{k-2}, t_{k-1})/6(\Delta t)^3 & \ldots l = k \end{cases} \tag{A4}$$

and

$$I_{cc}(\alpha, \beta, \gamma) = [F(\alpha, \beta, \gamma; t)\cos(\omega_n^* t) + G(\alpha, \beta, \gamma; t)\sin(\omega_n^* t)]|_{t_{k-3}}^{t_k} \tag{A5}$$

$$F(\alpha, \beta, \gamma; t) = \{-6 + [\alpha\beta + \beta\gamma + \gamma\alpha - 2(\alpha + \beta + \gamma)t + 3t^2](\omega_n^*)^2\}/(\omega_n^*)^4 \tag{A6}$$

$$G(\alpha, \beta, \gamma; t) = \{2(\alpha + \beta + \gamma) - \alpha\beta\gamma(\omega_n^*)^2[6 - (\alpha\beta + \beta\gamma + \gamma\alpha)(\omega_n^*)]t - (\alpha + \beta + \gamma)(\omega_n^* t)^2\}/(\omega_n^*)^3. \tag{A7}$$

The integral involving $\sin(\omega_n^* \tau)$ is evaluated similarly with similar outcome. The weights w_{kl}^{s} are given by eqns (A4) with "s" replacing "c" in the first two and "sc" replacing "c" in the last four equations. The quantity $I_{sc}(\alpha, \beta, \gamma)$ is given by

$$I_{sc}(\alpha, \beta, \gamma) = [-G(\alpha, \beta, \gamma; t)\cos(\omega_n^* t) + F(\alpha, \beta, \gamma; t)\sin(\omega_n^* t)]|_{t_{k-3}}^{t_k}. \tag{A8}$$

The weights w_{kl}^{i} are evaluated using a similar approach with the results being

$$w_{kl}^{i} = \begin{cases} w_{k-3,l}^{i} & \ldots 1 \leqslant l \leqslant k-4 \\ w_{k-3,k-3}^{i} + 39(\Delta t)^2/40 & \ldots l = k-3 \\ 27(\Delta t)^2/10 & \ldots l = k-2 \\ 27(\Delta t)^2/40 & \ldots l = k-1 \\ 3(\Delta t)^2/20 & \ldots l = k. \end{cases} \tag{A9}$$